Click Here for Full Article

A numerical approach to calculating soil wetness and evapotranspiration over large grid areas

P. J. Sellers,[1] M. J. Fennessy,[2] and R. E. Dickinson[3]

Received 11 April 2007; revised 5 June 2007; accepted 28 June 2007; published 20 September 2007.

[1] Soil wetness is typically highly variable in space over the length scales of general circulation model grid areas (~100 km), and the stress functions relating the surface evapotranspiration rate to local-scale (~1–100 m) soil wetness are very nonlinear. These two factors give rise to significant inaccuracies whenever a single grid area average soil wetness value is inserted into a stress function to calculate the evapotranspiration rate for a large grid area. A numerical method is presented to mitigate this problem. The distribution of soil wetness within a grid area is represented by binning, and a numerical integration of the stress function over this binned distribution provides a spatially integrated wetness stress term for the whole grid area, which permits calculation of grid area fluxes in a single operation. The method is very accurate when 10 or more bins are used. It can deal realistically with spatially variable precipitation, conserves moisture exactly, strongly reduces any oscillations, and allows for precise modification of the soil wetness distribution after every time step.

Citation: Sellers, P. J., M. J. Fennessy, and R. E. Dickinson (2007), A numerical approach to calculating soil wetness and evapotranspiration over large grid areas, *J. Geophys. Res.*, *112*, D18106, doi:10.1029/2007JD008781.

1. Introduction: The Scaling Problem

[2] Most climate general circulation models (GCMs) include models of the land surface and terrestrial biosphere [e.g., *Sellers et al.*, 1997; *Pitman*, 2003; *Yang*, 2004]. Treatment of subgrid-scale variability has been a perennial concern in calculating the fluxes of radiation, momentum, heat, water and CO_2 between the lower atmosphere and the land surface in these models. Typically, vegetation, terrain and soil wetness all vary on the scale of a few meters, while the length scale of a global GCM grid square is on the order of ~100 km. The use of finer GCM spatial resolutions may never close this difference in scale lengths and thus never explicitly resolve the variability in surface conditions. Other methods must be found to close the scale gap.

[3] *Sellers et al.* [1992a] presented an approach for defining the extent to which the scaling issue could be a problem for land surface properties and the calculation of associated large-scale fluxes. *Giorgi and Avissar* [1997] and *Nakaegawa et al.* [2000] also addressed this question through analysis. The numerical tests of *Sellers et al.* [1992a] assumed that the lower atmospheric forcing (downwelling radiation, temperature, humidity, wind speed) is relatively homogenous over a grid square at a given time and acts on a surface of varying vegetation density, slope and soil wetness. The tests showed that simple area-averaging schemes could be used to aggregate vegetation density and slope within a prairie-pasture field experiment domain (~30 km^2) with little impact on the accuracy of calculated fluxes of heat and moisture. Soil wetness, with its greater spatial variability [see, e.g., *Schmugge and Jackson*, 1996; *Ryu and Famiglietti*, 2006] and its associated nonlinear stress functions, was found to be more problematic. In this paper, we therefore concentrate on soil wetness as it is the subgrid-scale variable that represents the greatest challenge to scaling methodologies when calculating surface-atmosphere fluxes.

2. Scaling of Soil Moisture and Evapotranspiration to a Grid Average

[4] The surface water and energy balance of the land surface depends on many factors, including net radiation, precipitation and evapotranspiration, all of which may exhibit significant subgrid variability. In a GCM, these variations can be described using observational constraints but preferably such information should be provided by the internal dynamics of the moist processes in the climate model. In this paper, we explore a new method for accounting for the effects of such variations on the grid-averaged fluxes. In addition to the direct effects of spatial variability, there may be feedbacks between the subgrid-scale precipitation and soil moisture distributions, and a description of subgrid variations of surface runoff may also be included (for example, following the TOPMODEL approach of *Beven* [1989]), along with explicit treatments of the effects of variable water table depths [e.g., *Niu et al.*, 2007; *Miguez-Macho et al.*, 2007]. A complete description of soil moisture spatial variability also requires a treatment of the

[1] NASA Johnson Space Center, Houston, Texas, USA.
[2] Center for Ocean-Land-Atmosphere Studies, Calverton, Maryland, USA.
[3] Earth and Atmospheric Sciences, Georgia Institute of Technology, Atlanta, Georgia, USA.

Copyright 2007 by the American Geophysical Union.
0148-0227/07/2007JD008781$09.00

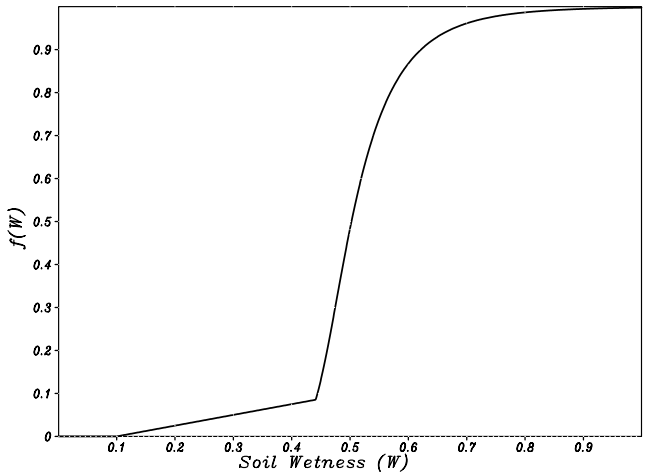

Figure 1. Relationship between the soil moisture stress function $f(W)$ and soil moisture W as used in this study (see equation (2)). This function is based on data presented by *Colello et al.* [1998] for the FIFE prairie grassland site in Kansas, USA.

subgrid distribution of snow depths and the meltwater contribution to the water balance, and a detailed description of how evapotranspiration is controlled by canopy resistances involving the tradeoffs between carbon assimilation and water loss, and the contribution of spatial distributions of canopy water storage and interception losses. We recognize that many such details would have to be included in any practical implementation of the method described in this paper within a climate model. However, the primary objective of this paper is not to develop such details but rather to demonstrate an approach for describing the dynamics of spatially and temporally varying soil moisture fields through integrations of a simple "toy model".

[5] Section 2.1 describes various approaches that can be used to estimate grid square average evapotranspiration rates, and introduces the concept of using fractional areas to describe the spatial distribution of soil moisture and thereby calculate more accurate time series of grid-scale fluxes and soil moisture. Section 2.2 shows how the equation for the local dynamics of soil moisture can be averaged to the grid square in terms of a partial differential equation for fractional area. It addresses in general terms all the process descriptions that might be so included and then simplifies to the toy model whose integrations are discussed in this paper.

2.1. Approaches to Scaling Evapotranspiration

[6] Potential evaporation, E_p, was early introduced as the evaporation rate in the absence of soil moisture stress. However, E_p is evidently not a fixed constant since it will depend on surface properties, net radiation, and surface temperature, through its dependence on the details of soil and canopy physiological processes, and in the shading of the former by the latter. For the purposes of this paper, it is convenient to take E_p as a fixed scaling parameter in mm d^{-1} and include any such variability as a multiplier, $f(C_i, S_i, R_i, T_i, q(z_j))$, where C_i are various canopy properties that might be included, S_i are various soil properties, T_i are temperatures of various components of the canopy and soil, R_i are various aspects of incident radiation, and $q(z)$ is the vertical distribution of soil moisture. Many of these dependences are sufficiently linear in their parameters that they can be obtained by use of grid square average properties with little loss of accuracy in obtaining a grid average as detailed in arguments given below. It is also assumed that the impact on evapotranspiration of the detailed vertical profile of soil moisture can be approximated by use of a single wetness parameter W.

[7] A grossly simplified representation of the dependency of the evaporation rate on this soil wetness will therefore be used to evaluate different scaling methods. At a given point within a GCM grid square, the local evaporation rate, E, is written as the product of the scaling parameter, E_p (mm d^{-1}), and a variable component whose dependence is limited to that on W, and designated as $f(W)$. This term can be viewed as representing soil water stress (i.e., reduction of root uptake resulting from drier soil) but may also include dependences on any other variables that can be correlated back to W, for example, those involving increases of temperatures resulting from increased soil dryness. Thus E is expressed as:

$$E = E_p f(W), \tag{1}$$

[8] An example of such a soil wetness stress function, $f(W)$, and used here for numerical computation, is that given by an analytic fit to local-scale (1–100 m) data presented by *Colello et al.* [1998]; that is,

$$f(W) = \mathrm{Max}\left(0.0; 0.25(W - 0.1); \tanh\left(0.0045\ q_s\ W^{-8}\right)\right) + 1.0, \tag{2a}$$

$$0 \le f(W) \le 1.0 \tag{2b}$$

where q_s (= −0.5 in this study) is the saturated soil moisture pressure, (Pa), and W is the local soil wetness ($0 < W < 1.0$). This expression is plotted in Figure 1. Many other authors [e.g., *Serraj et al.*, 1999; *Ronda et al.*, 2002] have inferred similar local-scale dependences of E on W.

[9] We can define the grid area evaporation rate by

$$E_I = E_p \int_A f(W) da \tag{3}$$

where E_I is the area-integrated value of E over the grid area domain A, and da is an elemental area within the domain. In method I of the tests described below, we integrate over the spatial variability in W (equation (3)) by subdividing the grid area into a very large number of cells (10^6). However, in the context of a GCM calculation, it is practically impossible to adequately resolve W over the domain and often soil moisture is represented by a single area-averaged value of W, $\langle W \rangle = \int_A W\, da$. This has been commonly used to estimate an area-averaged flux, E_A, by

$$E_A = E_p f(\langle W \rangle) \tag{4}$$

[10] Equation (4) is referred to as method II in the tests described below. Obviously, (4) is a much more economical calculation than (3). *Sellers et al.* [1992a] set out two conditions for which E_A will approach E_I and thus provide a realistic estimate of the grid-scale flux. (1) The independent function $f(W)$ is linear for the range of values of W found within the domain. This can be written as

$$\int_A abs\left[d^2 f(W)/d\ W^2\right] da \longrightarrow 0 \tag{5}$$

(2) The spatial variability of the independent variable (represented here by the standard deviation of the soil wetness, σ_W,) within the domain tends to zero:

$$\sigma_W \rightarrow 0 \tag{6}$$

[11] Area-averaged flux estimates, like E_A, will approach area-integrated fluxes, like E_I, as the product of (5) and (6) approaches zero. In practice, it has been shown that the dependence of evapotranspiration and/or photosynthesis on the vegetation parameter FPAR is nearly linear, and so (5) is almost satisfied when $f(W)$ is replaced by f(FPAR) [cf. *Sellers et al.*, 1992a, 1992b]. (FPAR is the fraction of photosynthetically active radiation absorbed by the vegetation canopy; grid-scale values of FPAR can be calculated from satellite observations at moderate spatial resolutions [see *Tucker et al.*, 1986; *Sellers et al.*, 1992b, 1996].) Effects of moderate topography may also be simply averaged [see *Sellers et al.*, 1992a]. However, both (5) and (6) are usually violated in the case of soil wetness because (1) $f(W)$ is highly nonlinear (see Figure 1), and (2) soil wetness, W, typically varies widely over length scales of a few meters to kilometers [e.g., *Ryu and Famiglietti*, 2006]. Thus E_A cannot be expected to provide a useful estimate of E_I (see also the simulation results of *Ronda et al.* [2002]). In addition, it will be shown that the use of equation (4) often leads to severe numerical oscillations in the calculated time series of E and W: during summer conditions, $\langle W \rangle$ can settle to the most nonlinear portion of the $f(W)$ function, $W \sim 0.45$ in Figure 1, and then respond violently to small changes in W due to convective rainfall events. (This is explored further in Appendix B, and Figures A1 and A2.)

[12] A different approach is to represent the soil wetness variability within A by a distribution function. The soil wetness W takes different values at different locations within A, but if we ignore the geographic location details of W, we can adequately describe these different values by "binning" them, that is, we can chose intervals, $W_j \leq W \leq W_{j+1}$ and associate a fractional area, a_j, with each interval. In the continuum limit of very small such intervals, we can write

$$\psi(W) = a_j/\left(W_{j+1} - W_j\right), \tag{7}$$

as a distribution function, to describe the soil moisture. Although we have inferred this distribution simply by neglect of spatial details in a deterministic problem, it is often convenient to use the tools of probability theory to further advance the theory of such distributions [e.g., *Rodriguez-Iturbe and Porporato*, 2004]. With soil water W as the independent variable, $da = \psi(W)dW$ so grid square averages can be obtained from

$$\langle () \rangle = \int_W ()\psi(W,t)dW. \tag{8}$$

[13] Many geographically fixed (e.g., topography and soils) or slowly varying properties (e.g., those of vegetation) can influence the fractional area that characterizes a particular W. If the collection of such properties is denoted K_i, then in general, the fractional area recognizing these different properties could be denoted $\psi(W, K_i)$ and if these properties are to be used to determine W, then equation (8) would have to be summed or integrated over these properties as outlined in the following section.

2.2. Scaling of Dynamical Soil Wetness

[14] If P denotes precipitation and R runoff, depending on local soil wetness, both in mm d^{-1}, then the time rate of change of soil moisture content in mm d^{-1}at a point is given by

$$S_{\max}\ d\ W/dt = P - E_p f(W) - R(W) \tag{9}$$

where $S_{\max}$ is the maximum soil moisture content, set equal to 100 mm in this study. A similar expression forms the basis for the analytical approaches of *Rodriguez-Iturbe and Porporato* [2004]. Climate models that include stomatal functioning and carbon assimilation commonly use more complex expressions for water balance than equation (9) [e.g., *Sellers et al.*, 1997]. However, the basic problems and solution techniques discussed in this paper will translate directly to these more complex models.

[15] The distribution term ψ introduced in equations (7) and (8) satisfies the equation for conservation of fractional area; that is, ψ (W) changes according to

$$\partial\psi/\partial t - \partial(D\psi)/\partial W = 0, \tag{10}$$

where $D(W) = (P - E) - R/S_{\max}$ is the "advection" or "drift" factor. Equation (10) is a 1-D scalar conservation equation. In other words, if we think of W as an independent variable coordinate space, then ψ remains unchanged in this space along the trajectory $W = (P - E - R)t/S_{\max}$. A new numerical technique (method III) is used to solve equation (10) (see below and Appendix A). As indicated, the fractional area ψ can be generalized to a multivariate distribution depending on all parameters that affect the change of soil moisture. The toy model presented in the next section only does this for two values of precipitation, i.e., 0 or a fixed value, but could easily be extended to cover more complex precipitation patterns, including those where the precipitation and soil moisture distributions may be coupled. The approach could also include multiple values of storage capacity $S_{\max}$ or runoff expressions $R(W)$, for example, from a fractional area of high versus low water table, or multiple expressions for $f(W)$, at relatively low computational cost.

[16] One other method is available to modelers. The domain may be divided up into a few subelements, or tiles, each of which contains its own water budget. Variations of this approach have been used by *Hahmann and Dickinson* [2001], *Koster et al.* [2000], *Gedney and Cox* [2003], and

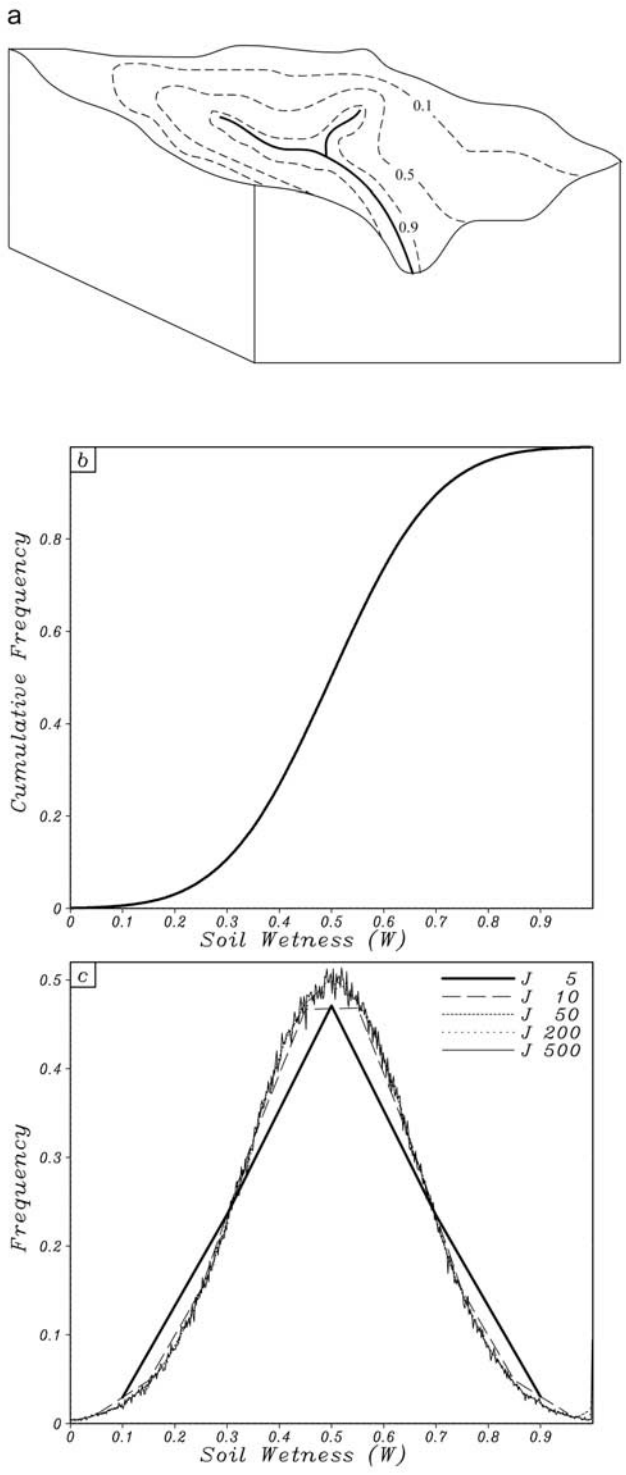

Figure 2. Different ways of representing soil moisture distributions within a GCM grid area: (a) soil wetness (W) contours in a grid area landscape, (b) soil wetness versus cumulative area, $a(W)$, (c) wetness distribution function (note that the y axis corresponds to fractional area). A normal distribution is shown centered on a mean value of $W = 0.5$. This distribution is used in this study as an initial condition, binned into $J = 5$, 10, 50, 200, and 500 bins. The numerical distributions have been normalized by the sum of $W_j a_j$, $j = 1, J$ for presentation.

Essery et al. [2003]. However, this approach (method IV) has significant limitations in representing the spatial variability of W (see Appendix B) and can give rise to severe excursions in the time series of W and E.

3. A Numerical Experiment to Evaluate Different Treatments of Soil Wetness Variability

[17] A numerical experiment was conducted to compare the performances of three different methods for estimating grid area evapotranspiration rates and the resultant time series of soil wetness.

3.1. Method I (Area Integrated)

[18] A grid area consisting of 10^6 individual cells was randomly initialized with a Gaussian soil wetness distribution (see Figure 2c). The grid area, which corresponds to the domain A in the equations above, was normalized to a unit area (1.0) to facilitate presentation of the results. Thereafter, a steady value of $E_p = 4.0$ mm d^{-1} was imposed with a 6 hour time step for 100 days. The evapotranspiration rate and change in soil wetness for each of the 10^6 cells was calculated using equations (1), (2), and (3). Rainfall events of 10 mm (area averaged) were imposed for the first time step of days 40 and 80, and these events were assumed to cover a randomly selected 20% of the cells in the grid area. For these cells, the rainfall intensity was set to 5 times (1/0.2) the area-averaged rainfall intensity. Runoff was generated wherever W exceeded a maximum wetness value, W_{max}. (W_{max} is close to 1.0 but is exactly defined in the explanation of method III below). For each time step, area-integrated mean and standard deviation statistics for soil wetness and evaporation rate were calculated using equation (4). No horizontal transfers were allowed between cells. In this study, we assume that this Monte-Carlo integration method gives us the most realistic soil wetness-evapotranspiration response as it explicitly resolves the spatial variation of soil wetness within a grid area. Results from method I are taken as the standard for judging the performance of the other methods.

3.2. Method II (Area Averaged)

[19] The initial soil wetness field from method I was averaged to give a single initial soil wetness value, $\langle W \rangle$ for the whole grid square, as is the normal practice in GCMs. Thereafter, equations (1), (3), and (5) were used to calculate the evaporation rates and soil wetness changes. Note that this is a single-point calculation for the grid area at each time step, instead of the 10^6 calculations of method I. The forcing and time step were the same as above, and rainfall was applied to 20% of the grid area, so that the local intensity for that 20% fraction was 5 times the area-averaged rainfall, as in method I. A separate calculation was then made for the wet 20% of the grid to determine the postrainfall local value of W, and runoff was generated whenever it exceeded W_{max}. The dry and wet fractions of the grid area were then recombined to give a single average value of $\langle W \rangle$ for the next time step.

3.3. Method III (Binned)

[20] Soil wetness within a grid area is represented by a distribution. Such a distribution can change from day to day

in a highly complex fashion, depending on the time history of evaporation and rainfall, so that analytical integration techniques commonly used to provide climatological statistics might be less useful in a GCM. Numerical techniques require us to approximate the continuous distribution into discrete elements, or bins. We propose a simple scheme whereby the total range of soil wetness values is binned into J bins of equal range (1.0/J), with one additional bin for areas with soil wetness identically equal to zero. (This last is a necessity for the numerical scheme to work). Thus for J = 10, we have ten bins with soil wetness ranges, W_j: = 0–0.1, 0.1–0.2, 0.2–0.3,. . .0.9–1.0, and one additional bin for W = 0. In each case we represent the average soil wetness in the bin by the midpoint of each range interval, so for J = 10 we have W_1 = 0.05, W_2 = 0.15, etc. The soil wetness distribution within the grid area is described by assigning fractional areas, a_j, to each bin (see Figure 2). Equation (10) can then be manipulated to a discrete form where changes in the soil wetness field are reflected by changes in a_j (see Appendix A for details).

[21] If the distribution of W within the domain A is known by a function, a (W); that is, the fraction of the area that has wetness of W or less (see Figure 2b), then the evapotranspiration rate for A as given by equation (1) can be calculated by integration over this distribution:

$$E = E_p\langle f(W)\rangle = E_p \int_A f(W)da \tag{11}$$

[22] With the bin discretization, the integral term in equation (11) is estimated by

$$\int_A f(W)da \sim \sum\nolimits_{\mathrm{j}=1}^{\mathrm{J}} f(W_j)a_j \tag{12}$$

where for brevity, the a_j is being used to represent the discrete bin increment (fractional area) of $a(W)$ for W between W_j and W_{j+1}.

[23] Insertion of equation (12) into equation (11) allows us to estimate the evapotranspiration rate for the grid area in a single operation. The result, E_B (B for binned or method III), will approach the exact solution, E, as J increases. The nonlinearity of the soil moisture term, $f(W)$, and the spatial variability of the soil moisture field, are both accounted for in equation (11). Once E_B has been calculated, the soil moisture distribution, a_j, must be updated to reflect evaporative losses and precipitation gains at the end of the time step. This is done by numerical integration of equation (10) (see Appendix A). Mass is exactly conserved.

[24] The advantage of using method III is obvious: the surface-atmosphere flux calculation only need be done once per grid area per time step, as has been done traditionally using E_A as given by method II in equation (5), but accuracy and realism are greatly improved. Typically, the surface-atmosphere flux calculation is expensive as the atmospheric column variable, surface prognostic variables and transfer coefficients embedded in E_p must be solved within a complex finite difference scheme to prevent numerical instabilities. The additional cost to the modeler in using method III versus method II is represented by (1) the need to preserve J (versus 1) prognostic soil wetness values per grid area, which is a computer storage burden, (2) the extra computation represented by equations (11) and (12), which is relatively trivial, and (3) updating the a_j at the end of each time step, which again is relatively trivial (see Appendix A).

[25] The initial soil wetness field from method I was sorted into the appropriate soil moisture bins to generate an initial numerical soil wetness distribution (see Figure 2c). Several bin totals (J) were used to test the effect of J on performance: J = 5, 10, 50, 200, and 500. Equations (11) and (12) were applied to calculate evaporation rates for each bin. Rainfall was assumed to cover 20% of each bin, which assumes that the landscape length scale, characterized by small-scale topography and local drainage, is much smaller than the length scale of moving precipitating storms. After a precipitation event the wet and dry fractions of each bin are treated separately to account for their differing contributions to the soil moisture distribution of the next time step.

[26] As with method I, no horizontal transfers between bins were calculated. Runoff was generated whenever W exceeded $W_{\max}$, the maximum storage value equivalent to the representative midbin value of the wettest (Jth) bin, $W_{\max} = (J - 0.5)/J$. Thus $W_{\max}$ varies with J. For a given method III test run with a selected value of J, the same value of $W_{\max}$ was used in the companion method I and method II runs to allow direct comparison of the results.

4. Results

[27] Figures 3 and 4 show the time variation of evaporation and soil wetness, respectively, calculated by the different methods over the 100 days. The method I and II trajectories are shown in all the panels, Figures 3a–3e and 4a–4e, while the results for method III for the different bin numbers J = 5, 10, 50, 200, and 500 are shown individually for comparison.

[28] In Figure 3a we see that method I and method II give very different trajectories for evaporation over time. Method I yields a higher evaporation rate over time and a more vigorous response to rainfall events than method II, as expected, because the wetter cells in method I contribute proportionately more to the total grid area flux when $\langle W\rangle$ is low. The effect of this on soil wetness can be seen in Figure 4a: the method I area-integrated soil moisture content dries out faster than the method II value. Figures 3a and 4a show the results for method III with a low value of J = 5; the soil wetness trajectory is initially simulated worse by method III than by method II; however, as we increase bin number, J,

Figure 3. Time variation of nondimensional grid area evaporation, i.e., $<f(W)>$, as calculated by the different methods over 100 days starting from the initial soil moisture condition shown in Figure 2c. (a)–(e) Methods I and II trajectories are shown, while the results for method III for the different bin numbers J = 5, 10, 50, 200, and 500 are shown individually for comparison. (f) The absolute errors in evaporation with respect to method I plotted against time for method II and for method III (all J values). (g) The absolute errors in grid area evaporation rate for selected days in Figure 3f plotted against bin number total J. Note how in all cases the method III evaporation error decreases with J.

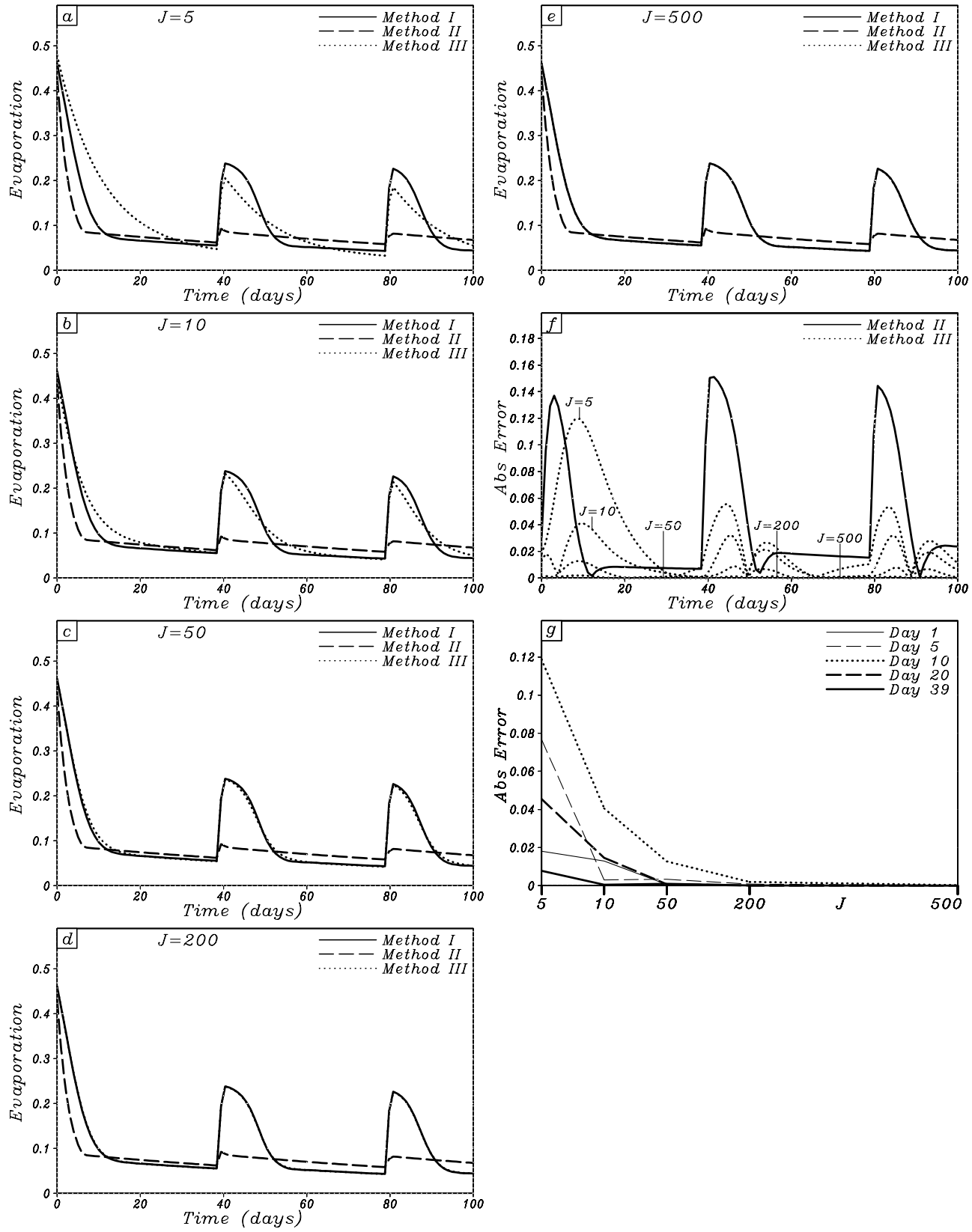
a
J=5
Method I
Method II
Method III
Evaporation
Time (days)
b
J=10
c
J=50
d
J=200
e
J=500
f
Abs Error
J=5
J=10
J=50
J=200
J=500
g
Day 1
Day 5
Day 10
Day 20
Day 39
J

Figure 3

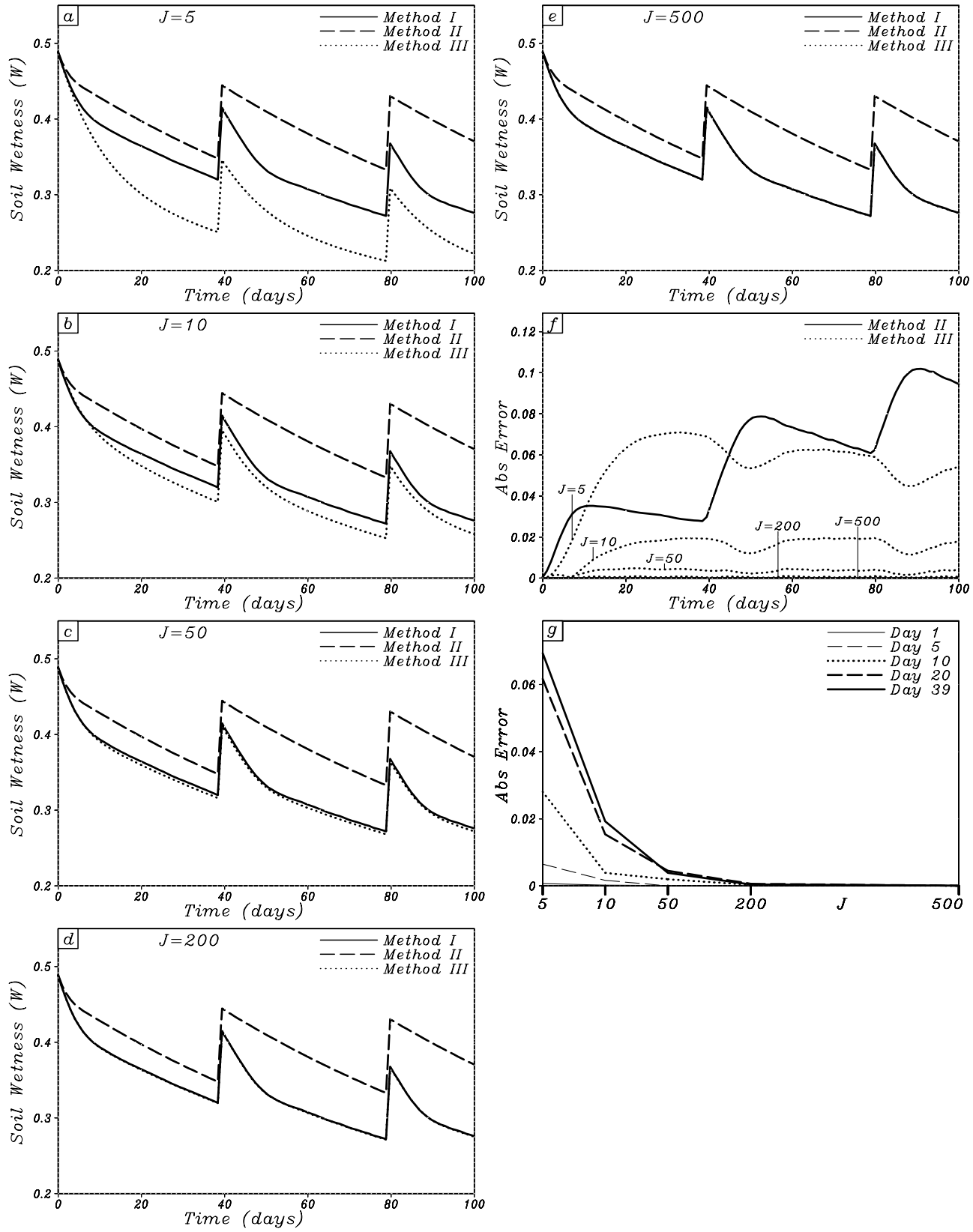

Figure 4. Time variation of grid area wetness as calculated by the different methods over 100 days. (a)–(e) Method I and II trajectories are shown, while the results for method III for the different bin numbers J = 5, 10, 50, 200, and 500 are shown individually for comparison. (f) The absolute errors in wetness with respect to method I plotted against time for method II and for method III (all J values). (g) The absolute errors in grid area wetness for selected days in Figure 4f plotted against bin number total J. Note how in all cases the method III wetness error decreases with J.

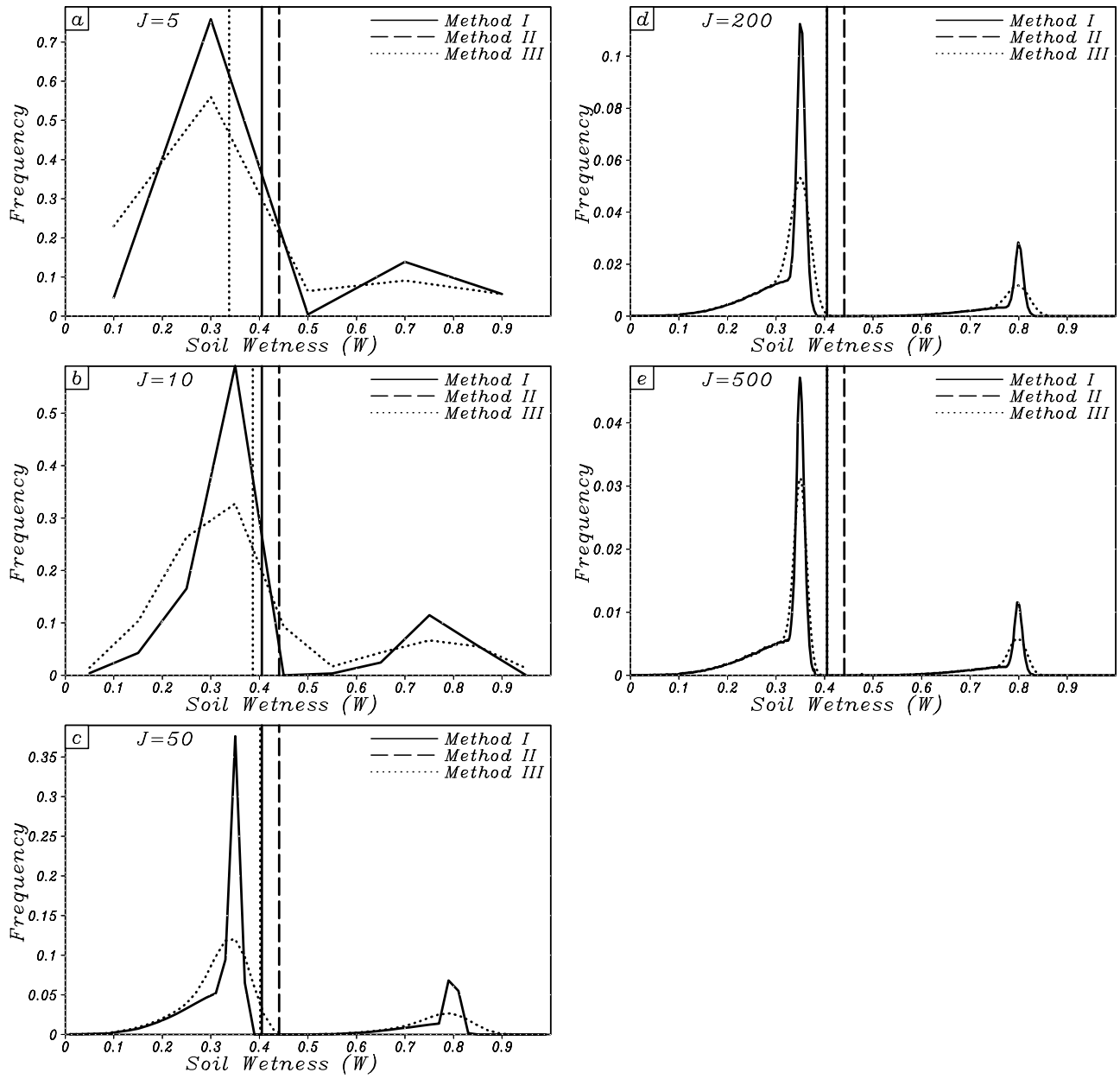

Figure 5. Soil wetness means and distributions calculated by methods I, II, and III for day 41, shortly after a rain event. The results show that as J is increased, method III produces a closer match in mean value and in overall distribution compared to method I. (a)–(e) Results for method III for J = 5, 10, 50, 200, and 500, respectively. In all cases, the method I results have been binned into the same J bins as method III to allow direct comparisons. Means calculated by each method are shown as vertical lines; where the method III line cannot be seen (Figures 5c, 5d, and 5e), the method I and method III means almost exactly overlap.

we see that method III rapidly converges on the solution of method I (see Figures 3a–3e and 4a–4e).

[29] The absolute errors (defined here as the absolute value of the difference between a method I value, which is taken as the "correct" standard, minus the equivalent method II or III values) in evaporation and wetness are plotted in Figures 3f and 4f against time for all values of J. Samples of the absolute errors shown in Figures 3f and 4f for specific days are plotted against J in Figures 3g and 4g. The rapid decrease in error with increasing J is obvious. For practical purposes therefore J = 10 is probably adequate, J = 50 is more than adequate, and J = 200 or 500 is overkill.

[30] Figures 5 and 6 show the calculated grid soil wetness distributions and means for days 41 and 81, with Figures 5a–5e and 5a–6e showing the effect of increasing J. The method I soil moisture distributions have been sorted into J corresponding bins for plotting so that we can directly compare the method I and III results for each value of J. Figures 5 and 6 show that as J is increased, the method III distribution more closely matches the results of method I. (Figures 5e and 6e provide good representations of the

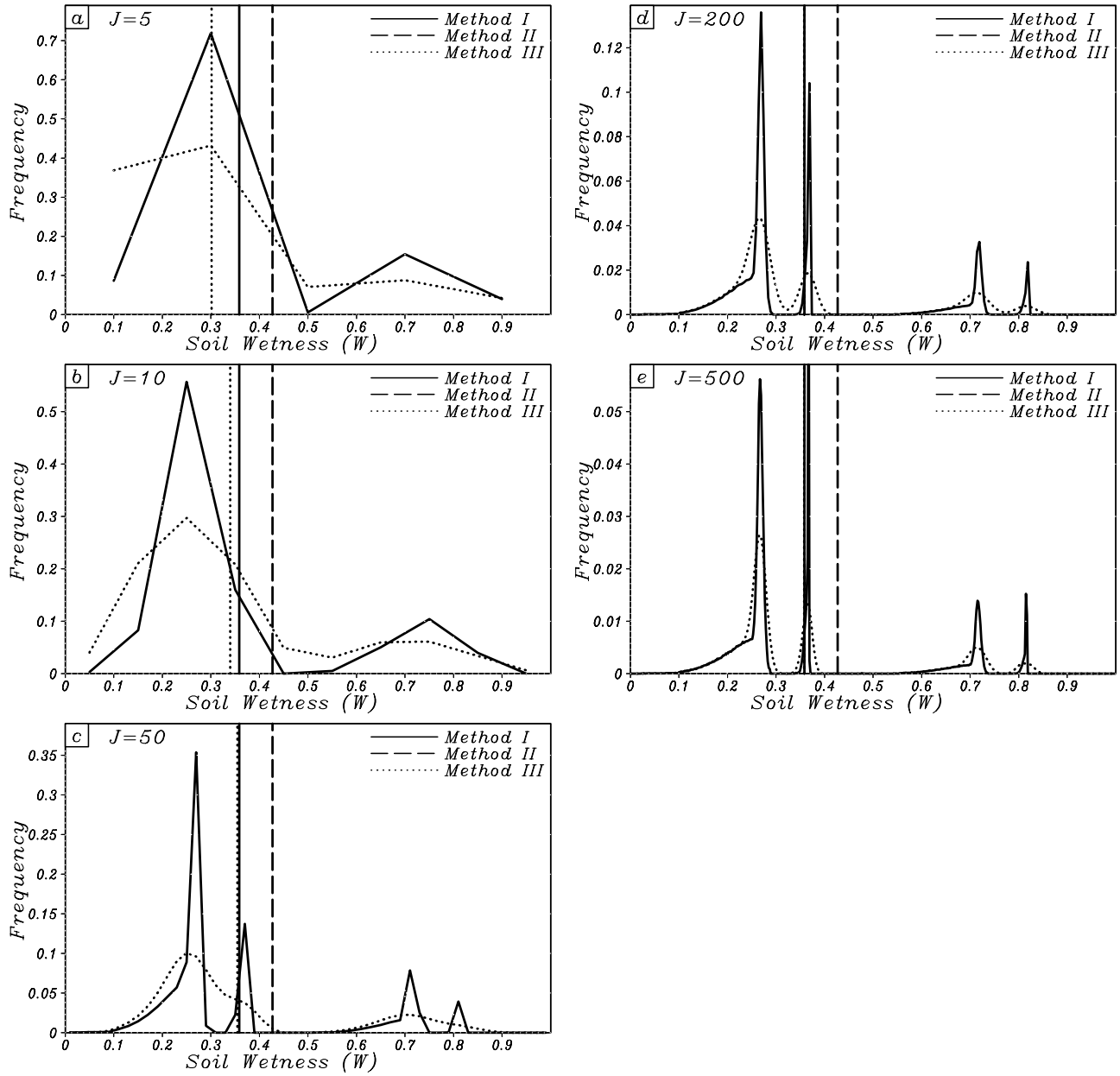

Figure 6. Soil wetness means and distributions calculated by methods I, II, and III for day 81, shortly after a rain event. The results show that as J is increased, method III produces a closer match in mean value and in overall distribution compared to method I. (a)–(e) Results for method III for J = 5, 10, 50, 200, and 500, respectively. In all cases, the method I results have been binned into the same J bins as method III to allow direct comparisons. Means calculated by each method are shown as vertical lines; where the method III line cannot be seen (Figures 6c, 6d, and 6e), the method I and method III means almost exactly overlap.

actual method I distributions as plotting the method I results into 500 bins is almost equivalent to full reproduction of the method I distribution.) The mean soil wetness values calculated by each method, equivalent to those plotted in Figure 4, are shown by vertical lines, where the method III means cannot be seen, in Figures 5c, 5d, and 5e and Figures 6c, 6d, and 6e, they almost exactly match the method I means. Figure 5 (day 41) shows that the method I soil moisture distribution is peaked around a value of around 0.35 and that method III reproduces this better as J increases. There is a secondary peak at around $W = 0.8$ resulting from the day 40 rain event. Figure 6 (day 81) shows similar results, with multiple peaks due to the effects of rain events combining with the existing soil moisture distributions in complex ways. Binning reduces the resolution in W, and so it is expected that binning will naturally tend to flatten out wetness peaks. Figures 5 and 6 show how the method III wetness peaks become flatter as J is decreased.

[31] Figures 7a and 7b show the changes in a simple soil moisture distribution during a drydown: the soil moisture peak moves to the left and becomes narrower, because the wetter areas in the distribution dry out faster than the dryer areas, which forces the right hand side of the wetness peak in Figures 7a and 7b to move to the left faster than the left hand side. Thus the standard deviation of wetness in a grid area will decrease during a drydown, as will the standard deviation of evapotranspiration. Figure 7c illustrates this effect for W: the standard deviation of W decreases with W, and W decreases with time during a drydown. As expected, these changes are better reproduced by method III with increasing J. In Figure 7d, analyses from a field experiment are shown for comparison; the standard deviation of the observed surface soil moisture over a 30 km^2 area is seen to decrease with time and with average soil moisture during a drydown [see *Sellers et al.*, 1992a]. Figure 7e shows how the simulated evaporation field also shows decreasing spatial variability during a drydown.

[32] Nonuniform rainfall events act to increase the spatial variability of soil wetness and evapotranspiration. With successive rainfall events, new "wet" peaks will be generated on the distribution graph; they will move from right to left as the area dries out, decelerating as they go; become narrower, and ultimately merge with the dryer peaks. This process can be seen at work in the simulated time series of soil wetness shown for method I and method III ($J = 500$) in Figure 8, and is apparent in the observations of *Ryu and Famiglietti* [2006].

5. Implementation of Method III Into GCM Land Surface Parameterizations

[33] The dependence of evaporation on soil wetness in equation (1) and Figure 1 is a highly idealized and simplified formulation. Several schemes describe the stress term $f(W)$ as a function of vegetation density and other factors, and calculate photosynthesis and evapotranspiration as interdependent quantities [see *Sellers et al.*, 1997]. Method III can accommodate these complexities. For example, if vegetation density is described as varying with soil moisture, we can rewrite equations (11) and (12) as

$$E_B = E_p \sum_{j=1}^{J} f(W_j).\Pi_j a_j \qquad (13)$$

where Π_j is the vegetation density parameter for the jth bin. ($\Pi_j = FPAR/k$ where k is a time-averaged extinction coefficient for PAR [see *Sellers et al.*, 1992b]). One approach is to confine vegetation to areas where the W_j values are above a certain threshold, equivalent to a soil moisture stress limit. Models using this approach can be initialized and validated using satellite-derived fields of Π [see *Tucker et al.*, 1986; *Sellers et al.*, 1996]. Also, climate models which incorporate method III could support prognostic vegetation which could be made dependent on the time history of the a_j field.

[34] As with equation (12), once the summation has been done in equation (13), the calculation of the grid area evaporation rate can be performed as a single operation. The same would apply for the calculation of canopy carbon fluxes, the contributions from complex landscapes can be done at marginal extra cost in computation.

[35] Horizontal moisture flow, base runoff and overland flow can be calculated using the soil wetness distribution in a number of ways. For example, the equation sets used in distributed hydrological models (see, e.g., the TOPMODEL of *Beven and Kirkby* [1979] and *Beven* [1989, and references therein]) can be adapted to use the bin framework. The horizontal flow, $R_{h(j,\,j-1)}$, between one bin and the next will be a function of their fractional areas (a_j and a_{j-1}), the difference in wetness ($W_j - W_{j-1}$), the topography, soil

Figure 7. (a) and (b) Change in a simple soil wetness distribution during a drydown as simulated over several days by method III for $J = 5$ and 500, respectively. Note how the peak moves to the left as the mean grid area soil moisture decreases and how the peak becomes narrower because the wet areas are evaporating faster than the dry areas. Thus the standard deviation of soil wetness decreases during a drydown. (c) Changes in the standard deviation of soil wetness, σ_W, during a simulated drydown. Each line represents a time history of σ_W versus soil wetness W moving from right to left as the drydown progresses. The method I and III simulations for days 1–39 shown in Figures 3 and 4 are presented here; note that the method III results converge on method I as total bin number J increases. (d) Results from a field experiment (FIFE-89) [from *Sellers et al.*, 1992a]. An airborne microwave radiometer was used to survey surface soil moisture W_S at ~90 m spatial resolution over several days during a drydown over an (30 km^2) area of mixed prairie grassland and pasture (data are from *Wang et al.* [1992]). The standard deviations of the surface soil moisture are plotted against the mean soil moisture content for the area, and the day numbers (day of year) are written against each data point. Note how soil moisture variability decreases with time and soil moisture (compare with Figure 7c). The line in the graph is a distributed model simulation result for the same period [see *Sellers et al.*, 1992a]. (e) Changes in the standard deviation of nondimensional evapotranspiration E during the same simulated drydown referred to in Figure 7a; again, note that the method III results converge on method I as J increases.

properties, etc. The base flow contribution from a bin, $R_{b(j)}$, will depend on W_j a_j; and overland flow, $R_{o(j)}$, will be a function of rainfall rate and the values of W_j a_j,

$$R_{h(j,j-1)} = f_1\left(a_j, a_{j-1}; W_j - W_{j-1}; topography : soils, etc.\right) \quad (14)$$

$$R_{b(j)} = f_2\left(a_j\ W_j; topography; soils, etc.\right) \quad (15)$$

$$R_{o(j)} = f_3\left(P, W_j\, a_j; topography; soils, etc.\right) \quad (16)$$

[36] Lastly, the effects of complex nonuniform rainfall may be worked into the bin method at little additional computational cost. In the tests described above, we defined the rainfall to be concentrated uniformly in a random 20% of the grid area, with the rest of the grid area staying dry during the time step. This amounts to a very simple soil wetness distribution of two bins. More complex rainfall distributions can be easily applied using the binning method

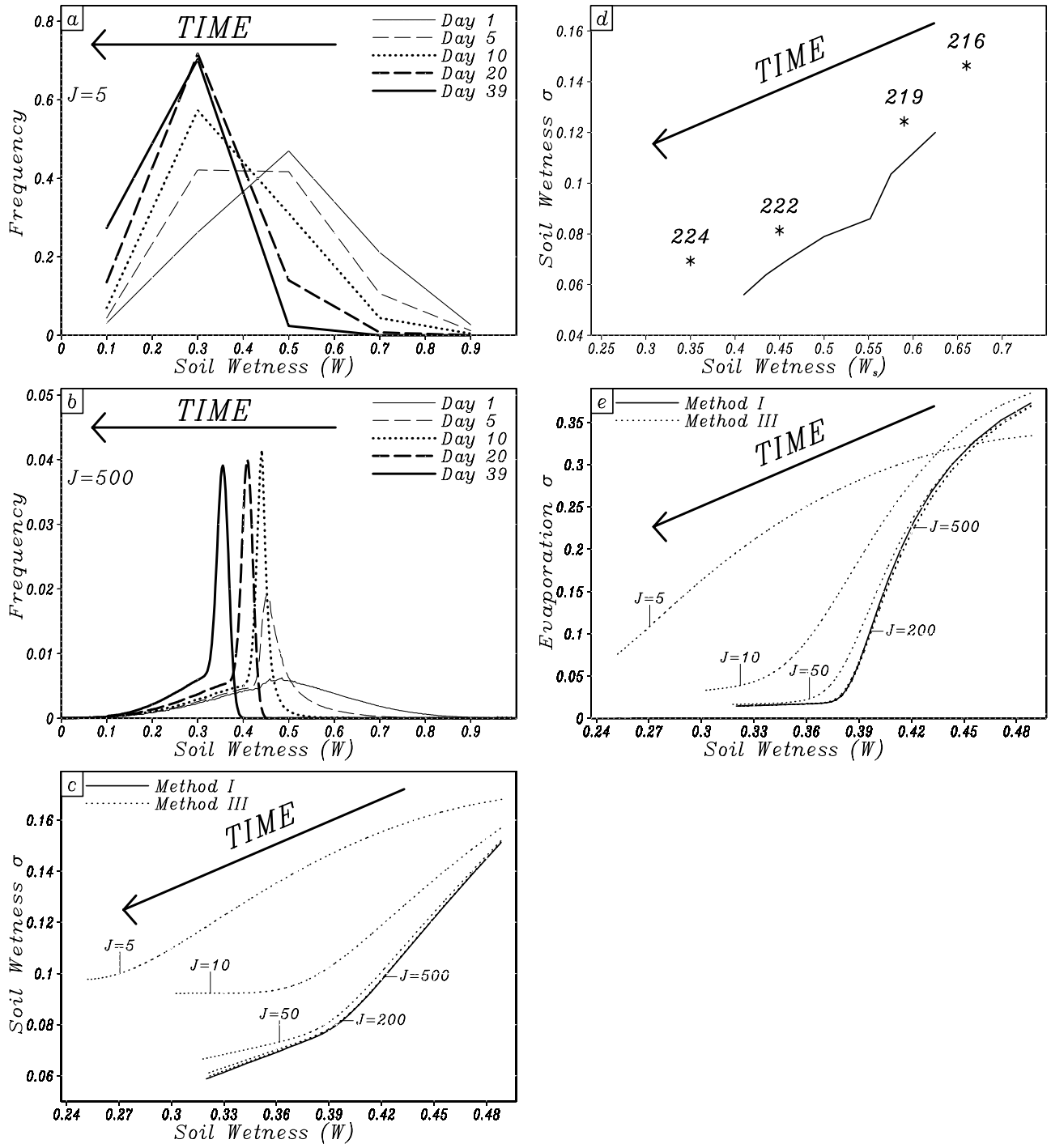

Figure 7

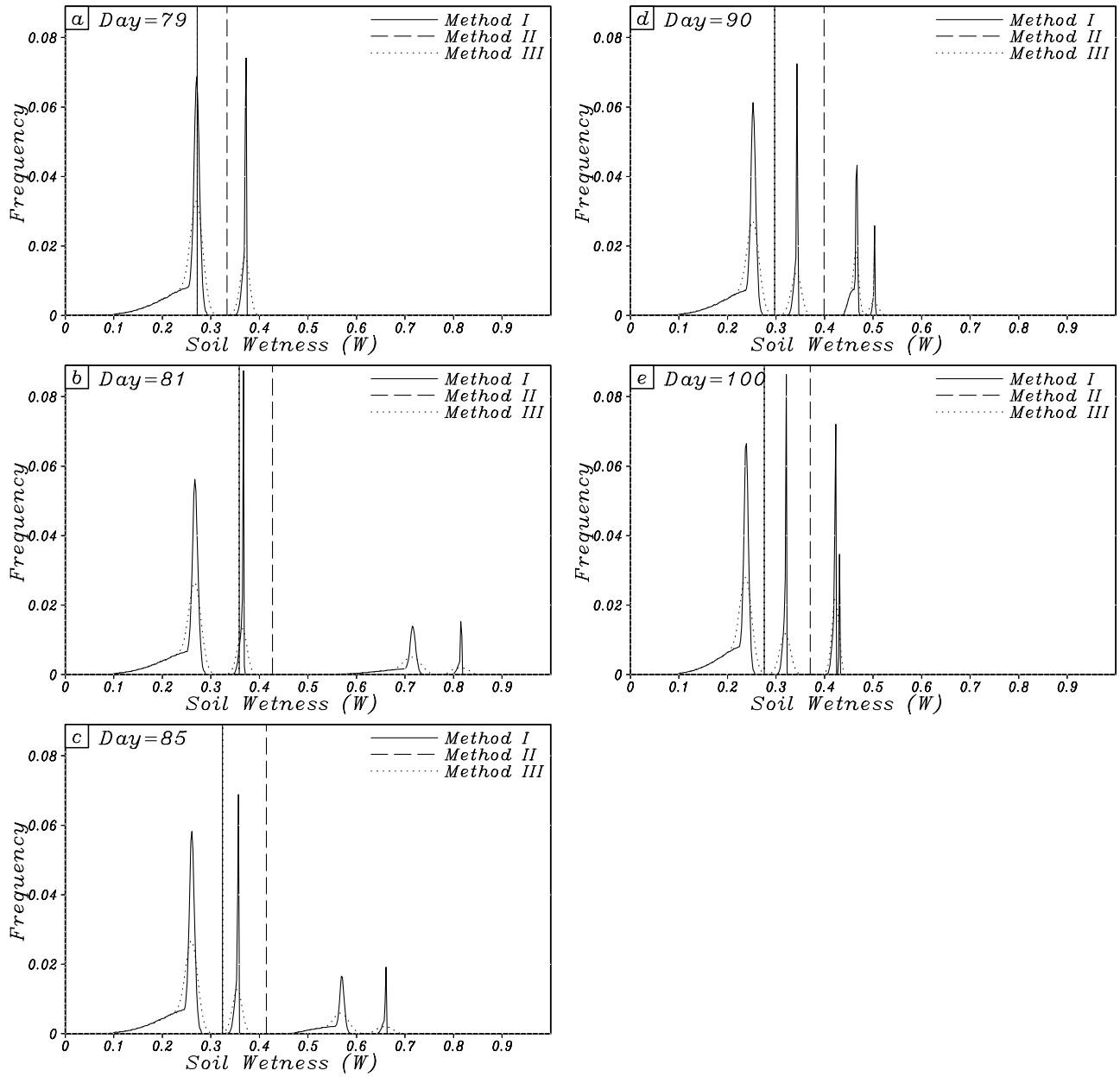

Figure 8. Time series of simulated method I and method III (J = 500) soil wetness distribution. (a) Distribution of soil moisture for day 79, at the end of a long drydown following the rain event of day 40 (see Figures 3 and 4). The two peaks correspond to (left) the initial day 1 wetness distribution and (right) the combination of the initial distribution and the day 40 rain event. (b) Day 81 soil wetness distributions (also shown in Figure 6e). The rain event of day 80 has combined with the day 79 distribution to produce two new "wet" peaks. (c)–(e) The wet peaks move to the left over the period of days 85, 90, and 100 and become narrower as they dry out (compare with observations of *Ryu and Famiglietti* [2006]). Ultimately, the two new "wet" peaks merge on day 100. Overall, the soil wetness variability has declined during the day 89–100 period. The method I and method III mean values are indistinguishable throughout.

by treating each bin as a temporarily separate area to which the rainfall distribution is applied (see Appendix A).

6. Summary and Future Directions

[37] Previous work has shown that simple area-averaging techniques for estimating surface-atmosphere fluxes will fail to provide accurate or realistic results when (1) the relationship between the dependent and independent variables is highly nonlinear and (2) the field of the independent variable shows high spatial variability over the domain of integration, i.e., does not satisfy equations (5) and (6). This is generally the case in nature for the relationship, $f(W)$, between evaporation rate, E, and soil wetness, W, over large

areas and can be a significant problem when calculating grid area moisture fluxes in GCMs.

[38] The soil wetness distribution within a grid area can be described using a simple binning approach, whereby the fractional areas, a_j, occupied by J wetness classes or bins can serve as a numerical analogue to the distribution. This fractional area, a_j, can then be used to integrate $f(W)$ over the grid area which allows a single but accurate calculation of total evaporative flux for the grid area. After each time step, a_j is adjusted to reflect evaporative losses or moisture gains from rain events. The method can be extended to describe other subgrid-scale moisture transfer processes, for example, horizontal soil subsurface flows, base flows, and overland flows; the separate contributions from vegetated and nonvegetated areas; and the effects of spatially variable rainfall. The method is exactly conservative of moisture. Around 10 bins seem to be adequate for accurately reproducing the grid area evapotranspiration rate.

[39] An alternative binning method (method IV) involves dividing up the grid area into a set of tiles or cells of fixed area, each with its own prognostic soil wetness value. This approach is equivalent to method I with a small number of cells. It is shown in Appendix B that this approach cannot realistically reproduce the effects of soil wetness variability unless a very large number of cells is used. In addition, this method is prone to large excursions in the calculated time series of E and W.

[40] The advantage of method III is that it involves almost no additional cost in computing large-scale surface-atmosphere transfers when compared to simple area-averaging techniques, which are unrealistic and inaccurate. There is a small computer storage burden in that 5−20 values must be retained for each grid area to define the spatial soil wetness distribution in place of the single area-averaged value $\langle W \rangle$ which is commonly used. The method can be used to define carbon fluxes in combination with evapotranspiration rates. The time history of changing spatial variability in soil wetness or vegetation can be realistically represented using method III which allows it to mesh well with satellite data analyses for initialization, validation and calibration.

[41] This modeling technique may also be useful in ecological applications where large-scale flux estimates must be calculated for areas with highly variable surface conditions using nonlinear formulations, for example in studies of large-scale carbon flows or trace gas dynamics.

Appendix A: Numerical Operation of Method III

[42] Equation (10) in the text defines the soil wetness as a distribution by

$$S_{\max}\partial\psi/\partial t - \partial(D\psi)/\partial W = 0, \tag{A1}$$

where $\psi(W) = \Delta a_j/\Delta W_j$, and $D = P - E(W)$. The distribution of W from 0 to 1.0 is discretized into J intervals $\Delta W_j = 1.0/J$, and the midpoint of these intervals is denoted W_j. Let an n superscript denote the nth time step. A time step is denoted Δt. Let $\lambda = D\Delta t/\Delta W$ and ΔI denote the integer nearest to but smaller than λ; that is, $\Delta I = int(\lambda)$. Then the fractional area at j will be moved in one time step to lie between $k = j + \Delta I$ and $k = j + \Delta I + 1$. That is, for P−E > 0, it will move to a larger value of W which can be referred to as "downstream". The numerical differencing of (A1) evaluated at the end of the time step has to be constructed to include these two neighboring points. When I is −1, as is normally the case for only E, the downstream points will be $j-1$ and j. For strong enough P, I can be nonzero and we can use the "strategy for extending solutions to long time steps" described by *Lin and Rood* [1996] with appropriate past references.

[43] With the binning method, equation (4) in the text is replaced by the sum

$$E_B = E_p \sum\nolimits_{\mathrm{j}=1}^{\mathrm{J}} f(W_j) a_j \tag{A2}$$

[44] Two conservation laws must be maintained: (1) conservation of relative area and (2) conservation of water. If we ignore runoff for the time being, these laws are expressed by

$$\sum\nolimits_{\mathrm{j}=1}^{\mathrm{J}} a_j = 1.0 \tag{A3}$$

$$\mathrm{d}/\mathrm{dt}\left[\sum\nolimits_{\mathrm{j}=1}^{\mathrm{J}} W_j a_j\right] = P - E_B \tag{A4}$$

[45] The specific steps used to solve (A1) in this study are as follows. Figure 2c shows how the soil wetness distribution of a grid area, $0.0 \le W \le 1.0$, is binned into J bins for method III, where the range of wetness in each bin is $1.0/J$, and the representative wetness of the jth bin is given by its midpoint wetness value

$$W_j = (j - 0.5)/J \tag{A5}$$

[46] Taking the simple case of evaporation and uniform rainfall, the change in W_j for a time step Δt is given by

$$\delta W_j = \left(-E_p f(W_j) + P\right)\Delta t \tag{A6}$$

This change δW_j must be incorporated into the distribution at $(t + \Delta t)$ as W_j is unchanging in this scheme, only a_j changes with moisture changes. To do this, we determine the bin values that bracket the new interim soil moisture content calculated for this bin, $W_j + \delta W_j$

$$W_k < W_j + \delta W_j < W_{k+1} \tag{A7}$$

A separate working array of b_k, $k = 1, J$ is defined and the b_k values initialized to zero at the beginning of each time step. In this array, $W_k = W_j$ so that the W_k soil wetness values correspond to the same W_j bin values as before, and b_k corresponds to the new fractional areas associated with them at $(t + \Delta t)$. Thereafter, as the evaporation rate of each bin is calculated using (A6) and (A7), the areas of its kth and $(k + 1)$th bins are incremented by

$$b_k = b_k + H\, a_j \tag{A8a}$$

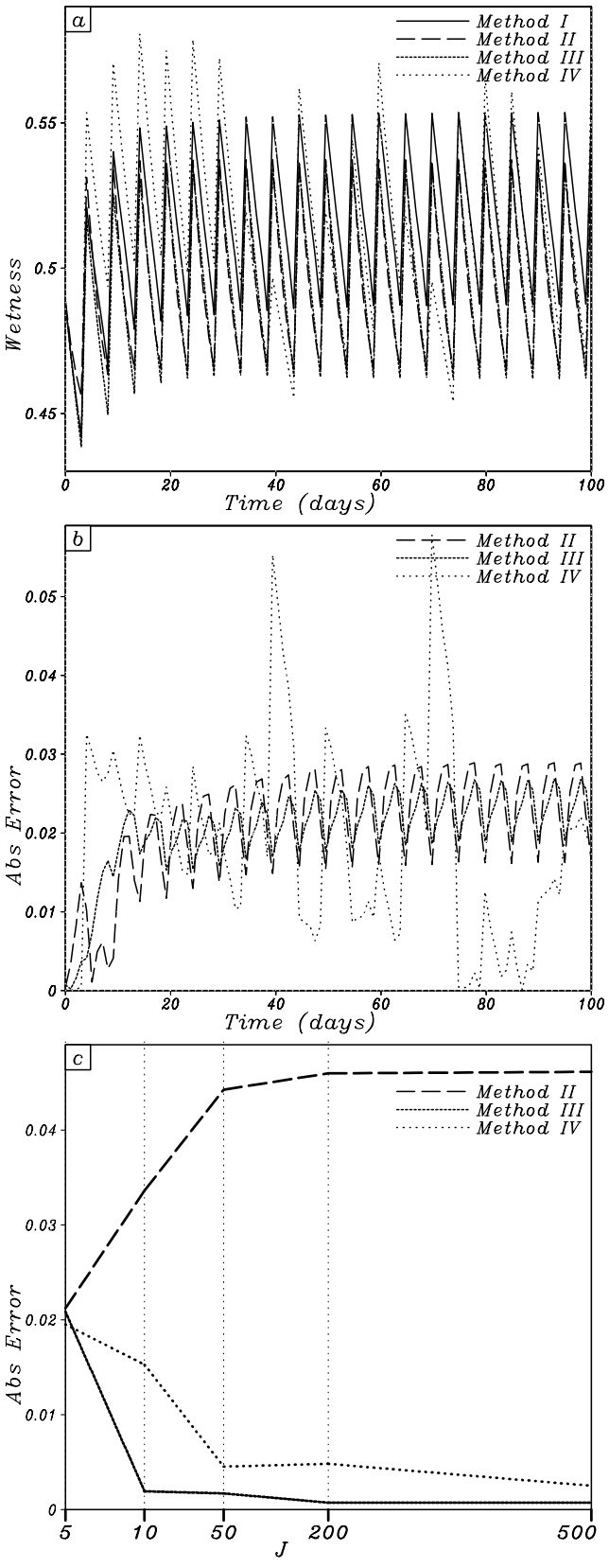

$$b_{k+1} = b_{k+1} + (1 - H)a_j \tag{A8b}$$

$$H = \big((W_j + \delta W_j) - W_k\big)/(W_{k+1} - W_k) \tag{A8c}$$

When equations (A6)–(A8) have been completed for all $j = 1, J$, the array b_k will contain the new soil wetness distribution for $(t + \Delta t)$; a_i $(j = 1, J)$ is then set to $b_k(k = 1, J)$ before the next time step. Mass (moisture) is exactly conserved. The equation set (A6)–(A8) must be run through J times to address all of the bins a_j.

[47] In the numerical experiment described in the paper, the rainfall was taken to be concentrated uniformly in one fraction, $h = 0.2$, of the grid area. Since we assume that the length scale of surface features and soil moisture variations is much smaller than the areas covered by a rainstorm in a time step, we can write separate equations for the wet and dry fractions of each bin a_j.

$$\delta W_{j(wet)} = \big(-E_p f\big(W_j\big) + P/h\big)h\Delta t \tag{A9a}$$

$$\delta W_{j(dry)} = \big(-E_p f\big(W_j\big)\big)(1 - h)\Delta t \tag{A9b}$$

where P is the area-averaged rainfall. The two equations (A9) are then run separately through (A7) and (A8) to increment b_k instead of (A6). Note that the wet and dry fractions will likely increment different b_k bins. To increment all the bins now requires $2J$ operations where the 2 refers to the wet and dry fractions in equation (A9). If we want to use a distribution for rainfall with L bins, we can write the grid area rainfall rate as

$$P = \sum\nolimits_{l=1}^{L} P_l c_l \tag{A10}$$

where P_l is the rainfall rate associated with a fractional area c_l. Equation (A9) can then be modified to a more general form

$$\delta W_{j,l,} = \big(-E_p f\big(W_j\big) + P_l\big)c_l\Delta t \tag{A11}$$

Figure B1. (a) Time variation of soil wetness as calculated using methods I, II, III, and IV for 100 days, with 20 mm rainfall events occurring every 5 days; $J = 5$ for methods III and IV. Note the large excursions in W calculated by method IV. (b) Variation in absolute errors (defined as the absolute value of the difference between the method I "standard" result and method II, III, and IV results for a time step) in calculated wetness over the 100 days; again, note the method IV excursions. (c) Plot of the absolute errors in wetness, integrated over the 100 days for each test of method III and IV, $N = 5$, 10, 50, 200, and 500 against J. Note how the performance of both methods improves as J increases but that method III performs significantly better than method IV. We initially expected that the error for method II would be a horizontal line, i.e., invariant with J; however, setting $W_{\max} = (J - 0.5)/J$ for all methods in the tests gives rise to a gradual change in the method II error with J.

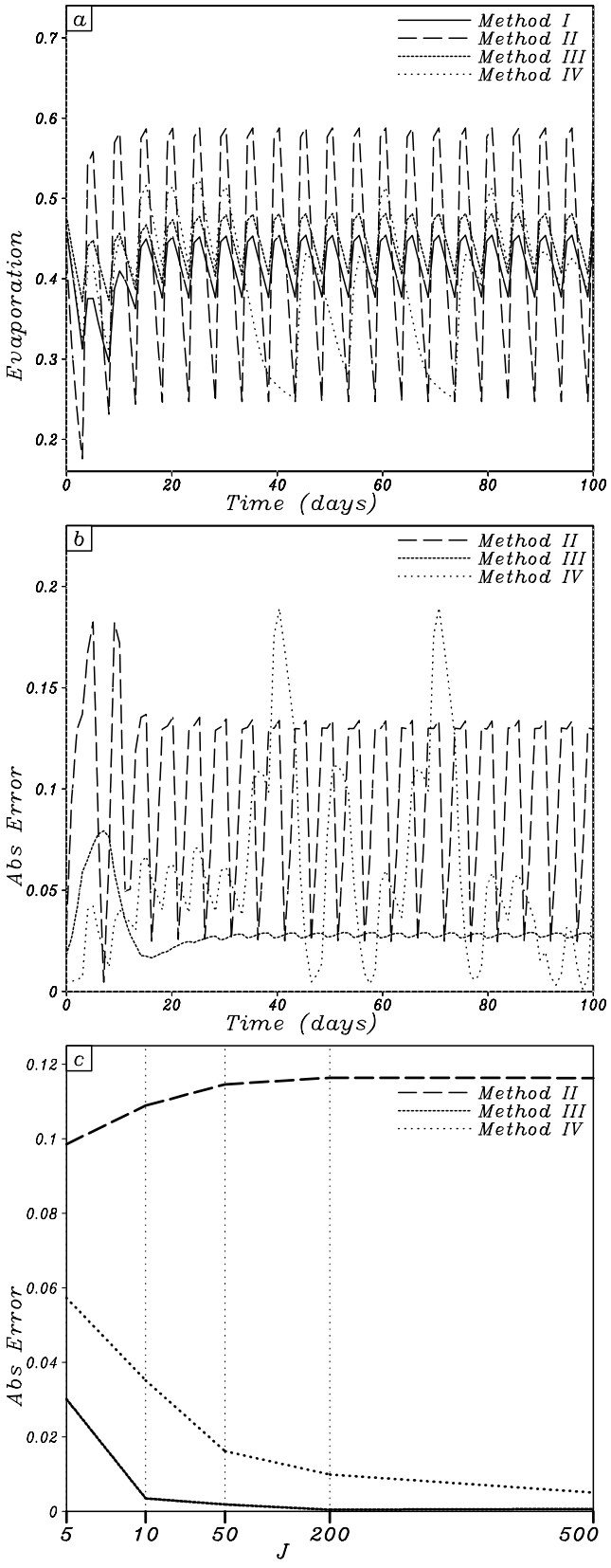

Equation (A11) can then be run through equations (A7) and (A8) as before, but now JL operations must be performed at each time step. It should be noted however that these are relatively cheap calculations compared to the work involved in calculating the nonintegral part of equation (11) in a GCM. Thus the method can be simply extended to handle multiple distributions interacting with each other.

Appendix B: An Alternative Binning Technique, Method IV

[48] Method III operates by changing the areas a_j associated with fixed W_j wetness values. An alternative binning approach can be used whereby a grid area is subdivided into J tiles or cells, each of fractional area $1/J$, and the wetness of each cell, W_j, allowed to vary according to equations (1), (2), and (3). This technique, method IV, is conceptually much simpler than method III and has the apparent advantage of allowing classification and separate treatment of different vegetation-soil complexes within a grid area. Mathematically, it is equivalent to method I except that a small number of cells are used.

[49] We have tested this approach against methods I, II, and III. The same range of cell totals, $J = 5$, 10, 50, 200, and 500 were used as for the method III tests. The initial value of the first method IV cell, W_1, was set by averaging the lowest $(10^6/J)$ method I W values; the second cell W_2 using the next lowest $(10^6/J)$ values, and so on. The initial soil moisture distribution of method I is better represented in method IV than in method III, as several of the initial a_j values in method III are initially set to almost zero, which amounts to a loss of information. The evaporation forcing was kept as before (E_p = 4 mm d^{-1}, with a 6 hour time step), and 20 mm of rainfall was applied every 5 days for 100 days.

[50] Figures B1a and B2a show the time variation of soil wetness and evaporation, respectively for all four methods for 100 days, where $J = 5$ for both methods III and IV. Very large excursions in the method IV evaporation rate can be clearly seen; these are due to the poor treatment of nonuniform rainfall by the few bins available. Also in Figure A2a,

Figure B2. (a) Time variation of nondimensional evapotranspiration as calculated using methods I, II, III, and IV for 100 days, with 20 mm rainfall events occurring every 5 days; J = 5 for methods III and IV. Note the large excursions in evapotranspiration calculated by method IV; also note the extreme oscillation in evapotranspiration calculated by method II under these conditions (see text for explanation). (b) Variation in absolute errors (defined as the absolute value of the difference between the method I "standard" result and method II, III, and IV results for a time step) in calculated evapotranspiration over the 100 days; the method II and IV excursions are more obvious. (c) Plot of the absolute errors in evapotranspiration, integrated over the 100 days for each test of method III and IV, $J = 5$, 10, 50, 200, and 500 against J. Note how the performance of both methods improves as J increases but that method III performs significantly better than method IV (roughly 10 times better for $J > 10$). The change in the error for method II with J is explained in the caption for Figure B1c.

we see that method II performs very poorly under these conditions, occasional nonuniform rainfall events typical of midcontinental summers, as the value of $\langle W \rangle$ settles to the most nonlinear part of the $f(W)$ curve, and the evaporation rate then oscillates between very high and very low values between rainfall events. We suspect that this may be an ongoing problem in several GCMs for continental summer conditions.

[51] Figures B1b and B2b show the time variation of the absolute error, as defined before for Figures 3 and 4, for wetness and evaporation, respectively, for methods II, III and IV over the time period. Again, the large departures calculated by method IV are obvious.

[52] Figures B1c and B2c show how the absolute errors integrated over the 100 days vary with J. As expected, both methods perform better as J increases, but method III always performs much better, by a factor of $\sim$10, than method IV. Method IV can only reproduce the "reality" of method I for very large J. It should also be remembered that method IV cannot deal with more complex rainfall distributions.

[53] **Acknowledgments.** This research was partially supported by DOE grant DE-FG02-01ER63198. The Center for Ocean-Land-Atmosphere Studies (COLA) and NASA/GSFC are thanked for providing facilities and support for some of this research. Randy Koster is thanked for both discussion of the final paper and a thorough and helpful critical review. The other reviewers are also thanked for their thoughtful and useful comments. Inez Fung and Forrest Hall are thanked for their discussions of the paper in its earlier phases.

References

Beven, K. J. (1989), Changing ideas in hydrology: The case of physically-based models, *J. Hydrol.*, *105*, 157–172.

Beven, K. J., and M. J. Kirkby (1979), A physically-based, variable contributing area model of basin hydrology, *Hydrol. Sci. Bull.*, *24*, 43–69.

Colello, G. D., C. Grivet, P. J. Sellers, and J. A. Berry (1998), Modeling of energy, water, and CO_2 flux in a temperate grassland ecosystem with SiB2: May–October 1987, *J. Atmos. Sci.*, *55*, 1141–1169.

Essery, R. L. H., M. J. Besst, R. A. Betts, and P. M. Cox (2003), Explicit representation of subgrid heterogeneity in a GCM land surface scheme, *J. Hydrol.*, *4*, 530–543.

Gedney, N., and P. M. Cox (2003), The sensitivity of global climate model simulations to the representation of soil moisture heterogeneity, *J. Hydrol.*, *4*, 1266–1275.

Giorgi, F., and R. Avissar (1997), Representation of heterogeneity effects in Earth system modeling: Experience from land surface modeling, *Rev. Geophys.*, *35*, 413–438.

Hahmann, A. N., and R. E. Dickinson (2001), A fine-mesh land approach for general circulation models and its impact on regional climate, *J. Clim.*, *14*, 1634–1646.

Koster, R. D., M. J. Suarez, A. Ducharne, M. Stieglitz, and P. Kumar (2000), A catchment-based approach to modeling land surface processes in a general circulation model, *J. Geophys. Res.*, *105*, 24,809–24,822.

Lin, S.-S., and R. Rood (1996), Multi-dimensional flux-form semi-Lagrangian transport schemes, *Mon. Weather Rev.*, *124*, 2046–2070.

Miguez-Macho, G., Y. Fan, C. P. Weaver, R. Walko, and A. Robock (2007), Incorporating water table dynamics in climate modeling: 2. Formulation, validation, and soil moisture simulation, *J. Geophys. Res.*, *112*, D13108, doi:10.1029/2006JD008112.

Nakaegawa, T., T. Oki, and K. Musiake (2000), The effects of heterogeneity within an area on areally averaged evaporation, *Hydrol. Processes*, *14*, 465–479.

Niu, G.-Y., Z.-L. Yang, R. E. Dickinson, L. E. Gulden, and H. Su (2007), Development of a simple groundwater model for use in climate models and evaluation with Gravity Recovery and Climate Experiment data, *J. Geophys. Res.*, *112*, D07103, doi:10.1029/2006JD007522.

Pitman, A. (2003), The evolution of, and revolution in, land surface schemes designed for climate models, *Int. J. Clim.*, *23*, 479–510.

Rodriguez-Iturbe, I., and A. Porporato (2004), *Ecohydrology of Water-Controlled Ecosystems—Soil Moisture and Plant Dynamics*, 442 pp., Cambridge Univ. Press, New York.

Ronda, R. J., B. J. J. M. Van Den Hurk, and A. A. M. Holtslag (2002), Spatial heterogeneity of the soil moisture content and its impact on surface flux densities and near-surface meteorology, *J. Hydrol.*, *3*, 556–570.

Ryu, D., and J. S. Famiglietti (2006), Multi-scale spatial correlation and scaling behavior of surface soil moisture, *Geophys. Res. Lett.*, *33*, L08404, doi:10.1029/2006GL025831.

Schmugge, T. J., and T. J. Jackson (1996), Soil moisture variability, in *Scaling Up in Hydrology Using Remote Sensing*, pp. 183–192, John Wiley, New York.

Sellers, P. J., M. D. Heiser, and F. G. Hall (1992a), Relations between surface conductance and spectral vegetation indices at intermediate (100 m^2 to 15 km^2) length scales, *J. Geophys. Res.*, *97*, 19,033–19,059.

Sellers, P. J., J. A. Berry, G. J. Collatz, C. B. Field, and F. G. Hall (1992b), Canopy reflectance, photosynthesis and transpiration. III. A reanalysis using improved models and a new canopy integration scheme, *Remote Sens. Environ.*, *42*, 187–216.

Sellers, P. J., S. O. Los, C. J. Tucker, C. O. Justice, D. A. Dazlich, G. J. Collatz, and D. A. Randall (1996), A revised land surface parameterization (SiB2) for atmospheric GCMs, part II: The generation of global fields of terrestrial biophysical parameters from satellite data, *J. Clim.*, *9*, 706–737.

Sellers, P. J., et al. (1997), Modeling the exchanges of energy, water and carbon between continents and the atmosphere, *Science*, *275*, 502–509.

Serraj, R., L. H. Allen, and T. P. Sinclair (1999), Soybean leaf growth and gas exchange response to drought under carbon dioxide enrichment, *Global Change Biol.*, *5*, 283–291.

Tucker, C. J., I. Y. Fung, C. D. Keeling, and R. H. Gammon (1986), Relationship between atmospheric CO_2 variations and a satellite-derived vegetation index, *Nature*, *319*, 195–199.

Wang, J. R., S. P. Gogenini, and J. Ampe (1992), Active and passive microwave measurements of soil moisture in FIFE, *J. Geophys. Res.*, *97*, 18,979–18,986.

Yang, Z.-L. (2004), Modeling land surface processes in short-term weather and climate studies, in *Observations, Theory, and Modeling of Atmospheric Variability*, *Ser. Meteorol. East Asia*, vol. 3, edited by X. Zhu, pp. 288–313, World Sci., Singapore.

R. E. Dickinson, Earth and Atmospheric Sciences, Georgia Institute of Technology, 311 Ferst Drive, Atlanta, GA 30332-0340, USA. (robted@eas.gatech.edu)

M. J. Fennessy, Center for Ocean-Land-Atmosphere Studies, 4041 Powder Mill Road, Suite 302, Calverton, MD 20705–3106, USA.

P. J. Sellers, NASA Johnson Space Center, Houston, TX 77059, USA.